Supporting information

Label-free high-throughput impedance-activated cell sorting

Kui Zhang ‡[ab], Ziyang Xia ‡[ab], Yiming Wang ‡[abc], Lisheng Zheng [ab], Baoqing Li *[ab] and Jiaru Chu *[ab]

[a.] Department of Precision Machinery and Precision Instrumentation, University of Science and Technology of China, Hefei, 230027, China. E-mail: bqli@ustc.edu.cn; jrchu@ustc.edu.cn

[b.] Key Laboratory of Precision Scientific Instrumentation of Anhui Higher Education Institutes, University of Science and Technology of China, Hefei, 230027, China

[c.] Biomedical Robotics Laboratory, School of Biomedical Engineering, Anhui Medical University, Hefei, Anhui, China, 230032.

‡ These authors contributed equally to this work.
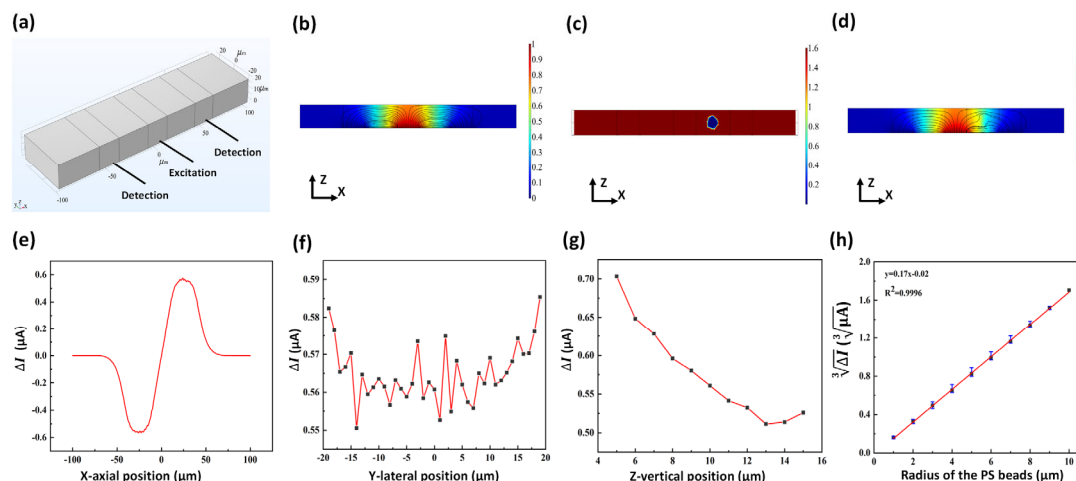
Section 1 Simulation of impedance detection

Fig. S1 Simulation of impedance detection. (a) Geometric modeling of microfluidic impedance detection. (b) Potential and electric field distribution in the absence of particle passage. (c) Conductivity distribution in the presence of particle passage. (d) Potential and electric field distribution in the presence of particle passage. All the above potentials are in V, and the streamlines indicate the electric field. (e) Influence of axial position on the impedance signal. (f) Influence of lateral position on the impedance signal. (g) Influence of vertical position on the impedance signal. (h) The third power of the radius of the PS beads is proportional to the impedance signal, and the error bars are the effect of position on the impedance signal.

COMSOL finite element simulations can be utilized to investigate the influence of particle position and size on the impedance signal. In Fig. S1a, the microchannel dimensions are 50 μm in width and 20 μm in height. The differential three-co-planar electrodes feature a width of 20 μm and a gap of 30 μm. The central electrode functions as the excitation electrode, while the electrodes flanking it serve as the detection electrodes. The default radius of the particles is 5 μm, and these particles consist of PS (polystyrene) beads suspended in a 1 × PBS buffer solution. The conductivity and relative permittivity of the PS beads are 5×10^{-6} S/m and 25, respectively. For the 1 × PBS buffer solution, the conductivity and relative permittivity are 1.6 S/m and 80, respectively. The excitation signal frequency is set at 500 kHz with an amplitude of 1 V.

In Fig. S1b, in the absence of particle passage, the electric field lines near the bottom electrode are more concentrated, whereas those farther from it are more dispersed, suggesting an uneven electric field along the height of the coplanar electrodes. Hence, microchannels with a narrowing height direction of the coplanar electrodes demonstrate improved impedance signals.

As particles pass through, their dielectric properties affect those of the microchannel, thereby influencing the detected current value. In Fig. S1c, the blue circular area represents the conductivity of PS beads, contrasting with the conductivity of the PBS solution outside the circle. This validates the accuracy of the material property definition method for both particles and the medium. In Fig. S1d, the electric field lines bypass the particle positions, indicating their insulating properties. This enables the impedance signal to accurately reflect the size characteristics of the particles.

In Fig. S1e, when only the x-axis position of the particle is altered while keeping other positions constant, a pair of interconnected peaks and valleys appears in the differential current. This effect occurs precisely at the midpoint between the two adjacent electrodes. Utilizing the times and distances of these peaks and valleys (with a 50 μm gap between electrode), it becomes possible to calculate the speed of the particle or cell in real-time. This method provides a simpler alternative to high-speed camera velocimetry, showcasing one of the advantages of impedance-activated cell sorting technology.

Since the particle radius is 5 μm, its effective transverse position spans from -20 μm to 20 μm, and its effective longitudinal position ranges from 5 μm to 15 μm. In Fig. S1f, when solely the y-transverse position of the particle fluctuates while other positions remain fixed, the differential current shows only minor fluctuations, remaining within the range of 0.03 μA. This outcome suggests that the coplanar electrode exhibits low sensitivity to variations in the particle's lateral position.

In Fig. S1g, when only the z-longitudinal position of the particles changes while other positions remain constant, the differential current exhibits significant fluctuations, reaching up to 0.2 μA. This sensitivity suggests that the coplanar electrodes respond to alterations in the particles' longitudinal position due to the non-uniformity of the electric field lines in the vertical direction. Additionally, as the distance from the bottom electrode increases, the differential current decreases. This pattern emerges because the electric field lines become less dense farther away from the bottom electrode, resulting in smaller variations in current. Therefore, it is crucial to design the microchannel height to match the diameter of the particles or cells. In this investigation, the channel height for chip preparation is set at 20 μm, considering the largest cell size, such as that of MDA-MB-231, with a diameter of approximately 20 μm.

In Fig. S1h, varying only the radius of the particle while keeping its position constant results in the current being proportional to the third power of the particle radius. Consequently, the magnitude of the impedance signal can be a dependable indicator for discriminating between particles of varying sizes.
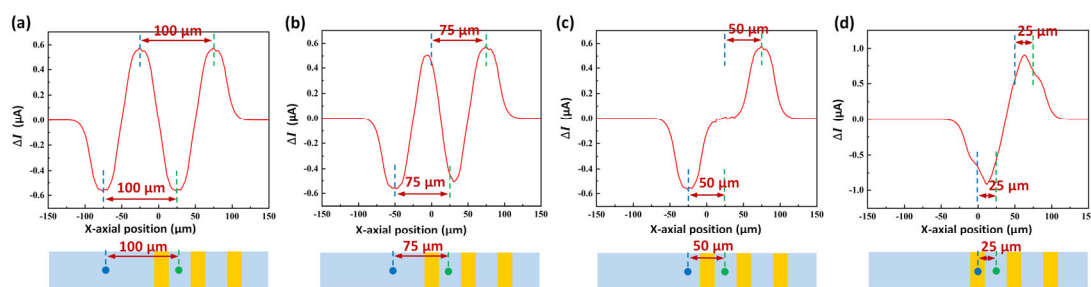
Section 2 The selection of cell concentration

Fig. S2 The influence of the distance between two adjacent particles, each with a diameter of 10 μm, on the impedance signal. The distances between two adjacent particles are (a) 100 μm, (b) 75 μm, (c) 50 μm, and (d) 25 μm, respectively. The electrode width is 20 μm, and the gap between two electrodes is 30 μm.

According to COMSOL finite element simulations, impedance signals with varying particle spacing can be generated. When the distance between two adjacent particles is 100 μm, exactly two complete peak-valley signals can be observed, as depicted in Fig. S2a. However, when this distance is reduced to 75 μm, the peak signal of one particle partially nullifies the valley signal of the other particle, leading to signal attenuation and positional offset, as illustrated in Fig. S2b. Moreover, when the distance between two adjacent particles is 50 μm, which equals the distance between the two gaps of the differential three-electrode system, the peak signal of one particle and the valley signal of the other particle cancel each other out. Consequently, two adjacent particles only produce a single pair of peak-valley signals, as shown in Fig. S2c. In contrast, when the distance between two adjacent particles is reduced to 25 μm, the distance between the two electrode gaps exceeds the distance between two adjacent particles. This causes the peak or valley signals of the two adjacent particles to overlap, resulting in a larger pair of peak-valley signals, as demonstrated in Fig. S2d. Therefore, based on these findings, the optimal distance between two adjacent particles is determined to be 100 μm.

To enhance the impedance signal for single-cell detection, it is essential to adjust the sample concentration to ensure that only one sample is present in the detection region. The concentration of cells is directly influenced by the distance between two adjacent cells. The subsequent discussion is divided into two parts: real-time high-throughput impedance detection and high-throughput sorting.

(1) Real-time high-throughput impedance detection

Because data acquisition and data processing are performed simultaneously, the distance between two adjacent cells (L) needs to satisfy the following formula:

$$L > T_{acq}v, L > T_{pro}v, L > D_{ele} \tag{S1}$$

Where T_{acq} is the time of impedance signal acquisition. T_{pro} is the time of impedance signal processing. D_{ele} is the distance of differential three-electrode. v is the sample flow velocity in the detection area. According to Fig. S2, D_{ele} is 100 μm, and L is greater than 100 μm.

Constrained by hardware limitations, the maximum sampling rate is 1 MSa/s. Assuming a sample flow velocity of 5 m/s, there are roughly 20 sampling points within 100 μm. Under these conditions, the T_{acq} and T_{pro} base on FPGA are 1 μs and 10 ns, respectively. According to formula (S1), the following conclusion can be drawn:

$$L > 100 \ \mu m. \tag{S2}$$

Therefore, we should ensure that the distance between two adjacent cells is greater than 100 μm. However, we cannot guarantee that all cells will be spaced more than 100 μm because the cells are randomly distributed in the microchannel. According to Poisson distribution[1], the single-cell detection efficiency (P) is equal to the probability that the distance between two adjacent cells is greater than 100 μm, which can be calculated using the following formula:

$$P = P(k = 0, \lambda) + P(k = 1, \lambda) \tag{S3}$$

Where $P(0,\lambda)$ is the probability of not containing cells within 100 μm. $P(1,\lambda)$ is the probability of containing one cell within 100 μm. They are calculated by the Poisson distribution formula:

$$P(k, \lambda) = \frac{\lambda^k e^{-\lambda}}{k!} \tag{S4}$$

Where k refers to the number of cells within 100 μm. λ is the average number of cells in the cell suspension, which is calculated by the following formula:

$$\lambda = CV \tag{S5}$$

Where C represents the concentration of cells. V is the sample flow volume corresponding to 100 μm, which is calculated as calculated by the following formula:

$$V = LWH = 6.67 \times 10^{-8} \ \text{mL} = 66.7\text{PL} \tag{S6}$$

Where W is the width of the sample flow in the detection area. According to the above formulas, the single-cell detection or sorting efficiency (P) can be described by the following formula:

$$P = (1 + CV)e^{-CV}. \tag{S7}$$

Assuming that the flow ratio of sheath flow and sample flow is 2 to 1, when the width of the microchannel is 100 μm, the width of the sample flow is approximately 33.33 μm. When the width of the microchannel is 50 μm, the width of the sample flow is approximately 16.67 μm. Here W is 33.33 μm. H is the height of the microchannel, which is equal to 20 μm. According to formula (S7), Fig. S3 can be drawn. The curve shows that as the concentration increases, the single-cell encapsulation efficiency first decreases slowly, then rapidly declines, and eventually approaches 0%. When the microchannel width is 100 μm or 50 μm in the detection area, the cell concentration in the real-time high-throughput impedance detection experiment is 3×10^6 cells/mL, which is equivalent to 98.25% or 99.53% of the theoretical single-cell detection efficiency, as shown in Fig. S3a & S3b.

(2) High-throughput sorting

Although each module of the system is carried out simultaneously, for the same cell, it needs to go through data acquisition, data processing and sorting response in sequence. Therefore, the distance between two adjacent cells (L) needs to satisfy the following formula:

$$L > (T_{acq})v, L > T_{pro}v, L > T_{sor}v, L > D_{ele} \tag{S8}$$

Where T_{acq} is the time of impedance signal acquisition. T_{pro} is the time of impedance signal processing. T_{pro} is the time of sorting response. v is the sample flow velocity in the detection area. D_{ele} is the distance of differential three-electrode. According to Fig. S1, D_{ele} is 100 μm, and L is greater than 100 μm.

Limited by the response frequency of the dual membrane pumps, the maximum sorting throughput is 1000 eps. Assuming a sample flow velocity of 1 m/s and a sampling rate of 230 kSa/s, there are approximately 23 sampling

points within 100 μm. In this condition, the T_{acq} and T_{pro} base on FPGA are 256 μs and 5 μs, respectively. T_{sor} is 1 ms. According to formula (S7), the following conclusion can be drawn:

$$L > 1,000 \ \mu m. \tag{S9}$$

According to formula(S6), the following conclusion can be drawn:

$$V = LWH = 6.67 \times 10^{-7} \ \text{mL} \tag{S10}$$

Where W is the width of the sample flow in the detection area. Assuming that the flow ratio of sheath flow and sample flow is 2 to 1, when the width of the microchannel is 100 μm, the width of the sample flow is approximately 33.33 μm. When the width of the microchannel is 50 μm, the width of the sample flow is approximately 16.67 μm. Here W is 33.33 μm. H is the height of the microchannel, which is equal to 20 μm.

According to formula (S7), Fig. S3 can be drawn. When the microchannel width is 100 μm or 50 μm in the detection area, the cell concentration in the high-throughput sorting experiment is 3×10^5 cells/mL, which is equivalent to 98.25% or 99.53% of the theoretical single-cell sorting efficiency, as shown in Fig. S3c & S3d.
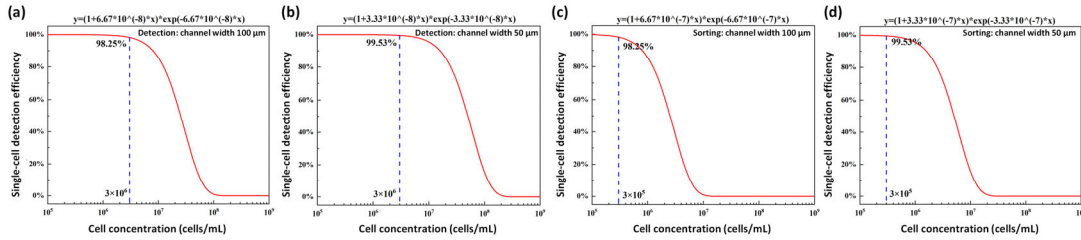

Fig. S3. The relationship between cell concentration and single-cell detection or sorting efficiency. (a, b) The correlation between single-cell detection efficiency and sample concentration is examined for microchannel widths of 100 μm and 50 μm, respectively. (c, d) The correlation between single-cell sorting efficiency and sample concentration is examined for microchannel widths of 100 μm and 50 μm, respectively.

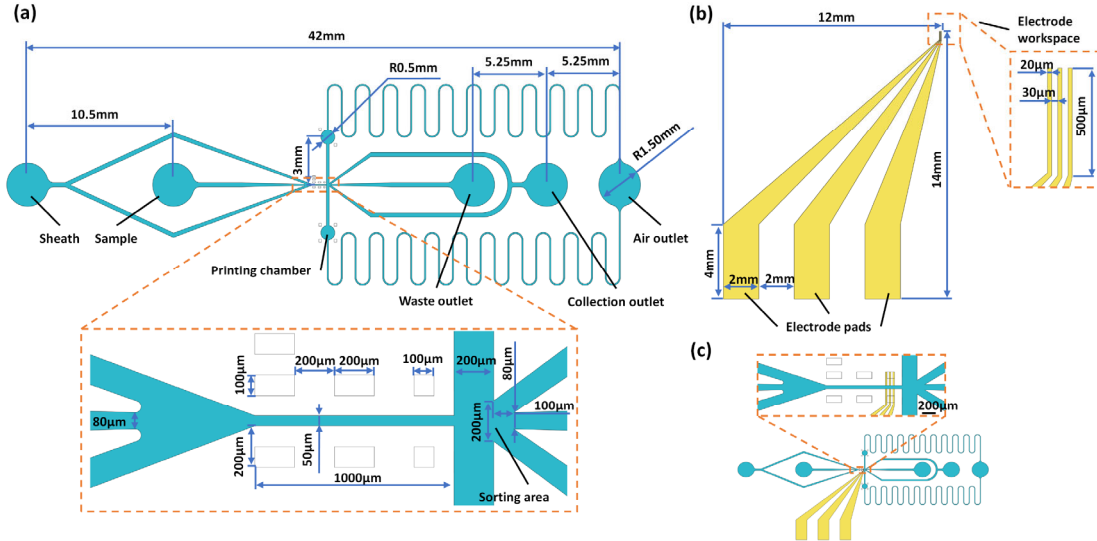## Section 3 Structural design and fabrication process of chip

Fig. S4 Structural design of chip. (a) Microchannel structure design of chip. (b) Electrode structure design of chip. (c) Overall layout of microchannel and electrodes.

The microchannel in the detection area has dimensions of 50 μm in width, 20 μm in height, and 1 mm in length, as illustrated in Fig. S4a. The electrodes have a width of 30 μm and a gap of 20 μm, as depicted in Fig. S4b. The distance from the electrodes to the sorting area is 100 μm, as shown in Fig. S4c.
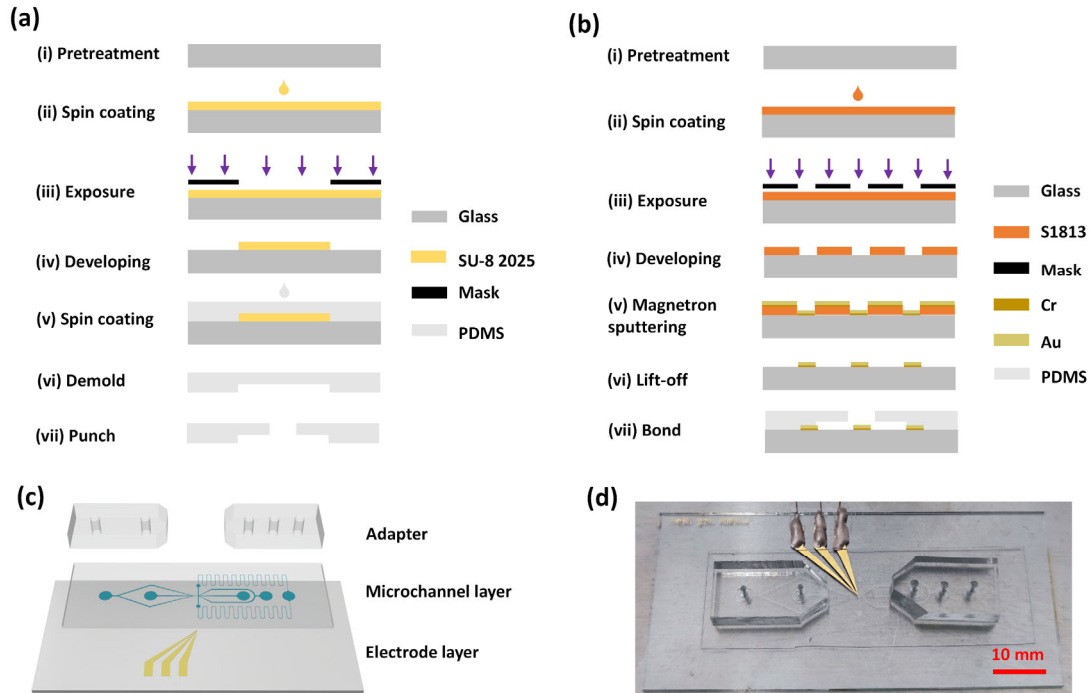
Fig. S5 Structure and fabrication process of the impedance-activated cell sorting chip. (a) Fabrication process of the microchannel layer. (b) Fabrication process of the electrode layer. (c) Schematic diagram illustrating the structure of the impedance-activated cell sorting chip. (d) Photograph showing the completed chip.

The fabrication process of the microchannel layer is depicted in Fig. S5a. (i) The borosilicate glass substrate underwent oxygen plasma treatment for 1 minute to effectively remove organic contaminants from its surface, enhancing surface activity and adhesiveness. (ii) SU-8 2025 negative photoresist was spin-coated onto the borosilicate glass substrate at a rotational speed of 3000 r/min for 30 s, resulting in a thickness of 20 μm. (iii) The substrate was exposed in a double-sided exposure machine (ABM/6/350/NUV/DCCD/BSIR/M, ABM, USA) for 10 s following pre-drying, where the substrate was heated at 65℃ for 3 min and 95℃ for 4 min. (iv) The substrate was immersed in the developer (PGMEA) for 150 s after post-drying, with the substrate being heated at 65℃ for 3 min, 95℃ for 1 min, and 65℃ for 3 min. (v) Upon completion of the soft lithography, the PDMS was mixed at a ratio of 10 to 1 and spin-coated onto the substrate at a rotational speed of 300 r/min for 30 s, resulting in a thickness of 300 μm. (vi) The substrate was heated in an oven at 65℃ for 2 hours, following which the microchannel layer was cut and stripped using a scalpel. (vii) Holes were drilled in the microchannel layer using a hole punch, and the layer was subsequently cleaned by immersion in acetone, ethanol, and deionized water.

The fabrication process of the electrode layer is illustrated in Fig. S5(b, i-vi). (i) The borosilicate glass substrate was treated with oxygen plasma for 1 minute. (ii) S1813 positive photoresist was spin-coated onto the borosilicate glass substrate at a rotational speed of 3000 r/min for 30 s, resulting in a thickness of 20 μm. (iii) The substrate was exposed in a double-sided exposure machine for 12 s after pre-drying, where the substrate was heated at 115℃ for 90 s. (iv) The substrate was developed in a developer (AZ300MIF) for 25 s. (v) Following post-drying, where the substrate was heated at 115℃ for 90 s, chromium and gold were sputtered onto the substrate using a magnetron sputtering platform (SP-SC4-A00, Syskey, China), with a thickness of 10 nm for chromium and 75 nm for gold. (vi) The substrate was soaked in acetone for 4 hours, and the photoresist was removed using a lift-off process to finalize the fabrication of the electrode layer. The electrodes had a width of 20 μm, and the spacing between neighboring electrodes was 30 μm. After subjecting the electrode layer and microchannel layer to oxygen plasma treatment, the microchannel and electrodes were aligned and bonded under a microscope, as demonstrated in Fig. S5(b, vii).

The impedance-activated cell sorting chip was manufactured using micro-electro-mechanical system (MEMS) techniques, comprising three main layers from bottom to top: the electrode layer, the microchannel layer, and the adapter, as depicted in Fig. S5c. The electrode layer was created on a borosilicate glass substrate using the lift-off technique. The microchannel layer was constructed with polydimethylsiloxane (PDMS, SYLGARD 184, Dow Corning, USA) using the soft lithography technique. The adapters were PDMS cubes with holes utilized for connecting with the cell suspension. The fabricated microfluidic chip is presented in Fig. S5d.

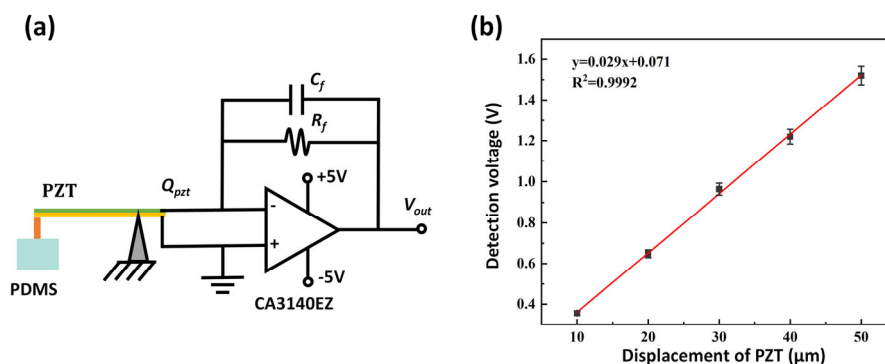## Section 4 Design of the dual membrane pumps

(a)

(b)

Fig. S6 PZT displacement detection. (a) Circuit schematic diagram of PZT displacement detection. (b) Voltage versus displacement measured using a three-dimensional moving table.

To mitigate the effect of PZT position errors on sorting and enable repeated experiments, it's essential to immobilize the PZT position. Here, the positive piezoelectric effect is employed to gauge the displacement of the PZT via charge amplification. The feedback resistance is 200 MΩ and the feedback capacitance is 100 pF, indicating a charge amplification of 10^{10}, as shown in Fig. S6a. A 10 µm displacement of the PZT results in a detected voltage change of approximately 290 mV, as shown in Fig. S6b. Alignment of the horizontal X and Y positions is first done under a microscope, followed by using the PZT displacement detection device to ensure that the distance between the piezoelectric actuator and the PDMS membrane is 10 µm.
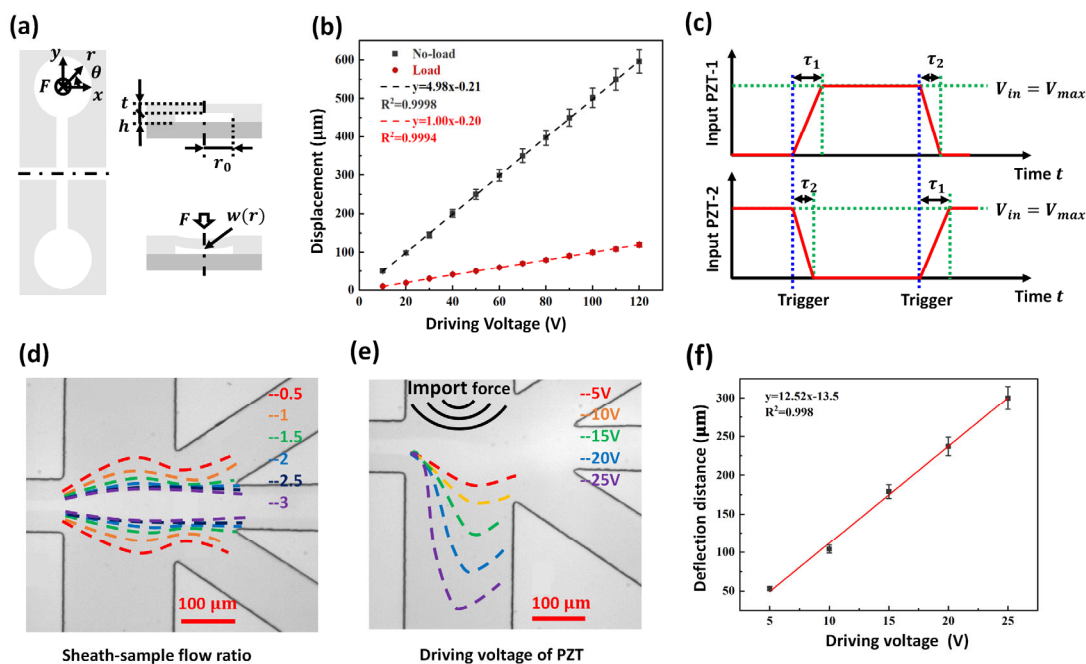
(a) **(b)** **(c)**

(d) **(e)** **(f)**

Fig. S7 Design of the dual membrane pumps. (a) Top and cross-sectional view of the dual membrane pumps. (b) The influence of the driving voltage on the displacement of the piezoelectric actuator under load and no-load conditions. (c) Voltage change during the simultaneous operation of dual membrane pumps. (d) Streamlines for different flow ratios of sheath and sample flow. (e) Streamlines for different driving voltages of the PZT. (f) The maximum deflection distance of the sample stream is proportional to the driving voltage.

The response frequency of the on-chip dual membrane pumps based on PDMS is related to the thickness (t) and displacement ($w(r)$) of the active membrane, material properties (such as E, μ, and ρ representing the Young's modulus, Poisson's ratio, and density of the active membrane, respectively), radius (r_0) and height (h) of the

printing chamber, and the magnitude (F) and position (r) of the driving force, as shown in Fig. S7a. The Young's modulus of PDMS is 2 MPa, Poisson's ratio is 0.45, and density is 1 g/cm^3. The thickness of the PDMS membrane is 300 μm, and the radius and height of the printing chamber are 500 μm and 20 μm, respectively. Fig. S7b shows the relationship between the driving voltage and displacement of the piezoelectric actuator when loaded (compressing the PDMS membrane) or unloaded. When the PZT starts to compress the PDMS membrane, an increase of 1 V in the driving voltage results in approximately 1 μm displacement of the PZT.

The control circuit of the on-chip dual membrane pumps is an RC charging circuit. The on-chip dual membrane pumps operate cooperatively; when the controller issues a trigger signal, one of the piezoelectric actuators is set to high voltage and the other to low voltage. When the next trigger signal arrives, the states of the two piezoelectric actuators are swapped. Here, τ_1 and τ_2 represent the rise and fall times of the driving voltage, respectively, and are 15 μs and 5 μs, as shown in Fig. S7c.

To ensure that cells pass through the waste chamber when the piezoelectric actuator is inactive, the flow rate ratio of sheath flow to sample flow should be set to 2:1, as shown in Fig. S7d. Different colored dashed lines in the figure represent streamlines under different flow rate ratios.

The displacement of the active membrane and the radius of the print chamber determine the size of the local flow, which in turn affects the deflection of cells in the sorting area. Thus, when the size of the print chamber and the position of the dual membrane pump are fixed, the drive voltage determines the cell deflection. As depicted in Fig. S7e, the dashed lines of various colors represent the flow lines at different voltages, with the optimal driving voltage being 10-15 V. At the same time, the maximum deflection distance of the sample stream is proportional to the driving voltage, as shown in Fig. S7f. At 10 V, the displacement of the PDMS membrane is approximately 10 μm, resulting in a local flow volume of about 7.8 nL. The length, width, and height of the sorting area are 200 μm, 250 μm, and 20 μm, respectively, resulting in a volume of 1 nL in the sorting area, where the local flow from the dual membrane pumps is sufficient to effectively deflect the cells under the main flow. When the driving voltage of the piezoelectric actuator is low, the cell deflection distance is insufficient for effective sorting. However, with a larger driving voltage, the cell deflection distance increases. Cells will enter the vertical local flow channels on both sides, but during the subsequent generation of the local flow, they will be directed into the collection channel on the closer side due to the combined effects of the local flow and the main flow.

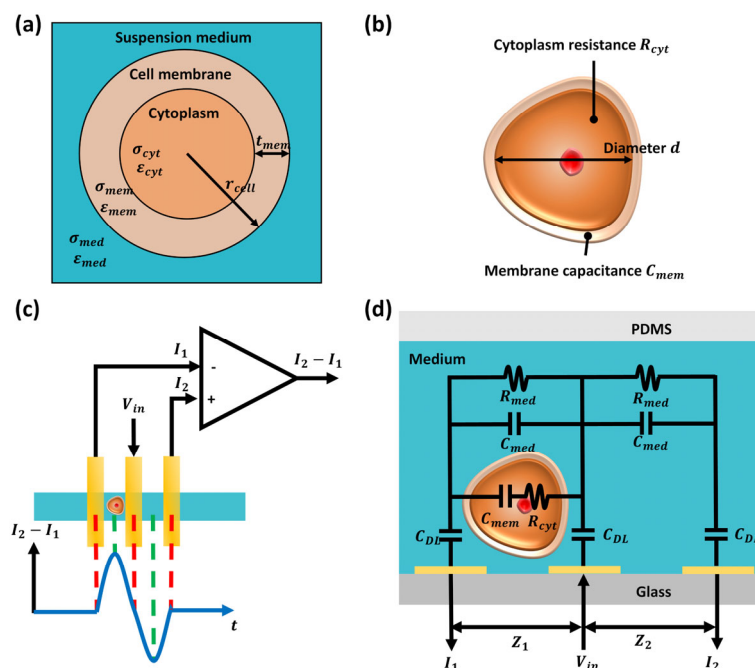## Section 5 Principle of impedance detection

Fig. S8 Principle of impedance detection[2]: (a) Single-shell model of the cell. (b) Electrochemical characterization of cells. (c) Differential three-electrode impedance detection model. (d) The equivalent circuit model of the differential three-electrode.

The single-shell model of the cell is divided into three layers: the suspension medium, the cell membrane, and the cytoplasm, as shown in Fig. S8a. Impedance signals of individual cells at different frequencies can express cell size and cell dielectric properties. Normalizing the cell impedance to bead impedance can be achieved using the following equation:

$$\tilde{f}_{CM}^{cell}\left(\frac{d_{cell}}{d_{bead}}\right)^3 = \tilde{f}_{CM}^{bead}\frac{A_{cell}}{A_{bead}} \tag{S11}$$

Where $\tilde{f}_{CM}^{cell}$ and $\tilde{f}_{CM}^{bead}$ are the Clausius-Mossotti factors for the cell and bead, respectively. d_{cell} and d_{bead} are the diameter of the cell and bead, respectively. A_{cell} and A_{bead} are the measured impedance signal amplitudes for the cell and bead, respectively. Here $\tilde{f}_{CM}^{bead}$ and d_{bead} are known values, whereas $\tilde{f}_{CM}^{cell}$ and d_{cell} are unknowns to be determined. The Clausius-Mossotti factor for the cell can be determined by the following equation:

$$\tilde{f}_{CM}^{cell} = \frac{\tilde{\varepsilon}_{cell} - \tilde{\varepsilon}_{med}}{\tilde{\varepsilon}_{cell} + 2\tilde{\varepsilon}_{med}} \tag{S12}$$

Where $\tilde{\varepsilon}_{med}$ is the complex permittivity of the medium, and $\tilde{\varepsilon}_{cell}$ is the complex permittivity of the cell. Assuming the cell is a single-shell model, $\tilde{\varepsilon}_{cell}$ can be determined by the following equation:

$$\tilde{\varepsilon}_{cell} = \tilde{\varepsilon}_{mem}\frac{\gamma^3 + 2\left(\frac{\tilde{\varepsilon}_{cyt} - \tilde{\varepsilon}_{mem}}{\tilde{\varepsilon}_{cyt} + 2\tilde{\varepsilon}_{mem}}\right)}{\gamma^3 - \left(\frac{\tilde{\varepsilon}_{cyt} - \tilde{\varepsilon}_{mem}}{\tilde{\varepsilon}_{cyt} + 2\tilde{\varepsilon}_{mem}}\right)}, \gamma = \frac{r}{r - t_{mem}}, \tilde{\varepsilon} = \varepsilon + \frac{\sigma}{j\omega} \tag{S13}$$

Where $\tilde{\varepsilon}_{mem}$ and $\tilde{\varepsilon}_{cyt}$ are the complex permittivities of the cell membrane and cytoplasm, respectively. t_{mem} is the thickness of the cell membrane, r is the radius of the cell, and ω is the angular frequency. The Clausius-Mossotti factor and impedance spectrum vary with small perturbations in the electrical properties of cells. Due to the high resistance of the cell membrane, at low AC frequencies (<1MHz), cells behave as insulating particles ($\tilde{f}_{CM}^{cell} = \tilde{f}_{CM}^{bead}$). Therefore, low-frequency impedance signals directly reflect the volume of the cell.

According to the single-shell model of the cell, the electrochemical characterization of cells, including cell diameter, cell membrane capacitance and cytoplasmic resistance, can be obtained by particle calibration, as shown in Fig. S8b. A dual-frequency excitation signal is applied to the center electrode of the differential three-electrode and impedance signals are collected from both side electrodes, as shown in Fig. S8c. The equivalent circuit model of the differential three-electrode configuration includes cell membrane capacitance (C_{mem}), cytoplasmic resistance (R_{cyt}), capacitance of the medium (C_{med}), resistance of the medium (R_{med}), and electric double-layer capacitance (C_{DL}), as shown in Fig. S8d. When a cell passes through, changes in impedance in the detection area lead to alterations in current. In the differential three coplanar electrode configuration, assuming one pair of electrodes is used to measure the impedance Z_1 of the cell-medium mixture, and the other pair of electrodes is exclusively employed to measure the impedance Z_2 of the medium. Z_1 and Z_2 can be determined by the following expressions:

$$\begin{cases} Z_1 = \dfrac{2}{jwC_{DL}} + \dfrac{R_{med}\left(1 + jwR_{cyt}C_{mem}\right)}{jwR_{med}C_{mem} + \left(1 + jwR_{cyt}C_{mem}\right)\left(1 + jwR_{med}C_{med}\right)} \\ \qquad Z_2 = \dfrac{2}{jwC_{DL}} + \dfrac{R_{med}}{\left(1 + jwR_{med}C_{med}\right)} \end{cases} \tag{S14}$$

Compared to the two coplanar electrode model, the differential three-electrode coplanar electrode model can reduce environmental noise, enhance signal-to-noise ratio, and improve sensitivity. In the differential three coplanar electrode model, the differential current ($I_2 - I_1$) can be obtained. After transimpedance amplification, the weak current signal is converted into a voltage signal and amplified. I_1、I_2、U_1 and U_2 can be determined by the following expressions:

$$\begin{cases} I_1 = \dfrac{V_{in}}{Z_1}, I_2 = \dfrac{V_{in}}{Z_2} \\ U_1 = R_1 * G_1 * I_1, U_2 = R_2 * G_2 * I_2 \\ \Delta U = U_2 - U_1 \end{cases} \tag{S15}$$

Where R_1 and R_2 represent the transimpedance gains, G_1 and G_2 represent the output voltage gains, V_{in} is the excitation voltage, and ΔU is the differential voltage. If $R_1 = R_2 = R, G_1 = G_2 = G$, the above expression can be simplified to:

$$\Delta U = R * G * V_{in} * \left(\frac{1}{Z_2} - \frac{1}{Z_1}\right). \tag{S16}$$

The excitation voltage ($S(t)$) consists of an alternating current voltage ($A = 1\,V$) at two frequencies ($\omega_1 = 500\,kHz$ and $\omega_2 = 5\,MHz$), which can be expressed as the following equation:

$$S(t) = A \cos \omega_n t, \quad n = 1, 2. \tag{S17}$$

Under the voltage excitation, the output signal of the impedance cytometry is denoted as $O(t)$, which can be demodulated to in-phase ($X(t)$, also known as real part) and quadrature ($Y(t)$, also known as imaginary part) components by two demodulators in the lock-in amplifier. $O(t)$, $X(t)$ and $Y(t)$ can be respectively determined by the following equations:

$$\begin{cases} O(t) = A_n \cos(\omega_n t + \theta_n) \\ X_n(t) = O(t) \times \cos \omega_n t \quad , \qquad n = 1, 2 \\ Y_n(t) = O(t) \times \sin \omega_n t \end{cases} \tag{S18}$$

where A is the amplitude of the impedance signal, θ is the phase. If there is no cell in the detection area, the magnitude and phase of the impedance signal is constant. When a cell passes through the electrodes, it changes the conductivity of the detection area and causes impedance pulses in the impedance signal. The magnitude (A) and phase (θ) of impedance pulses belong to the dielectric properties of single cell.

$$\begin{cases} A_n = \sqrt{X_n^2 + Y_n^2} \\ \theta_n = \mathrm{atan}\left(\dfrac{Y}{X}\right) \end{cases} , \qquad n = 1, 2. \tag{S19}$$

According to the principle of impedance detection and the equivalent circuit model, the relationship between the impedance signal and the cell characteristics can be derived, which is of great significance in guiding the optimization of experimental process parameters.
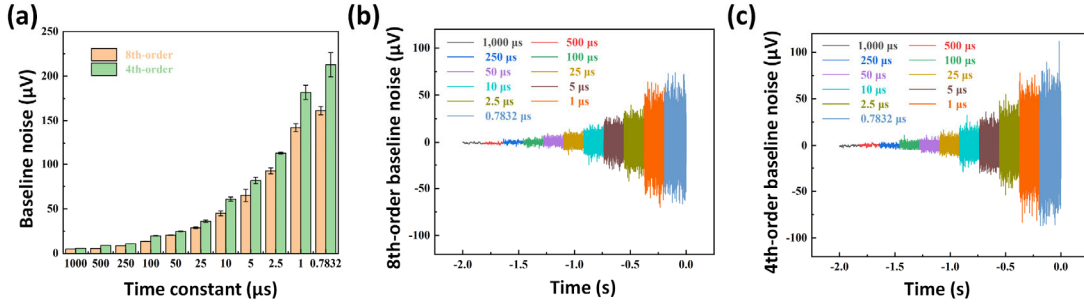
Section 6 Parameter settings

Fig. S9 Baseline noise versus time constants. (a) Baseline noise at different time constants for 8th and 4th order low-pass filters. (b) and (c) are baseline noise at different time constants for 8th-order and 4th-order low-pass filters, respectively.

To enhance impedance signals and sorting effects, it is crucial to investigate pertinent parameters related to impedance detection and sorting. For a given time constant, a higher-order low-pass filter results in reduced baseline noise and a smoother fitted curve. Hence, an 8th-order low-pass filter was chosen for the experiment, as depicted in Fig. S9a. Additionally, for a fixed low-pass filter order, a smaller time constant leads to increased baseline noise, as illustrated in Fig. S9b & S9c.

Based on the setting of the time constant (TC) of the 8th-order low-pass filter, its 95% stabilization time (τ), and cutoff frequency (f_{-3dB}) can be calculated by the following formula:

$$\begin{cases} \tau = 13 * TC \\ f_{-3dB} = \dfrac{0.0479}{TC}. \end{cases} \tag{S20}$$

The flow velocity upper limit (v_{max}) under different time constants can be calculated by the following formula:

$$v_{max} = \frac{D_{ele\_gap}}{\tau} \tag{S21}$$

Where D_{ele_gap} is the gap distance of the differential three electrodes. Here, D_{ele_gap} is 50 μm. τ is the 95% stabilization time of the 8th-order low-pass filter.

The impedance velocimetry error primarily stems from the sampling rate, given the high linearity and dimensional accuracy of the electrodes prepared using the chromium mask version, which results in a fabrication error smaller than the error attributed to the sampling rate. Assuming that the sampling rate (f_{Sa}) is the sampling

rate when the impedance velocimetry error is ±5%, 10 sampling points are needed in the electrode gap distance of 50 μm, and the reference formula is as follows:

$$f_{Sa} = \frac{10}{\tau}. \tag{S22}$$

According to the formula (S20, S21, S22), the parameter settings of lock-in amplifier can be summarized, as shown in Table S1. The maximum sampling rate based on DAC transmission can reach 1 MSa/s.

Table S1 Parameter settings of lock-in amplifier

TC (μs)	τ (μs)	f_{-3dB} (Hz)	v_{max} (m/s)	f_{Sa} (kSa/s)
1,000	13,000	48	0.004	0.769
500	6,500	96	0.008	1.538
250	3,250	192	0.015	3.077
100	1,300	479	0.038	7.692
50	650	958	0.077	15.385
25	325	1,916	0.154	30.769
10	130	4,790	0.385	76.923
5	65	9,580	0.769	153.846
2.5	33	19,160	1.538	307.692
1	13	47,900	3.846	769.231
0.7832	10	61,159	4.911	982.164

As shown in Table S1, the parameters relevant to impedance detection are correlated with the sample flow velocity. Hence, measuring the sample flow velocity is necessary to determine these impedance detection parameters. Common velocity prediction methods in the field of cell sorting include optical velocimetry, image velocimetry, impedance velocimetry, and predictions based on pressure and flow resistance when using pressure pumps, as well as predictions based on flow rate and microchannel cross-sectional area when using syringe pumps. Given that this system utilizes syringe pumps and impedance detection, it is feasible to employ either impedance velocimetry or flow velocimetry.
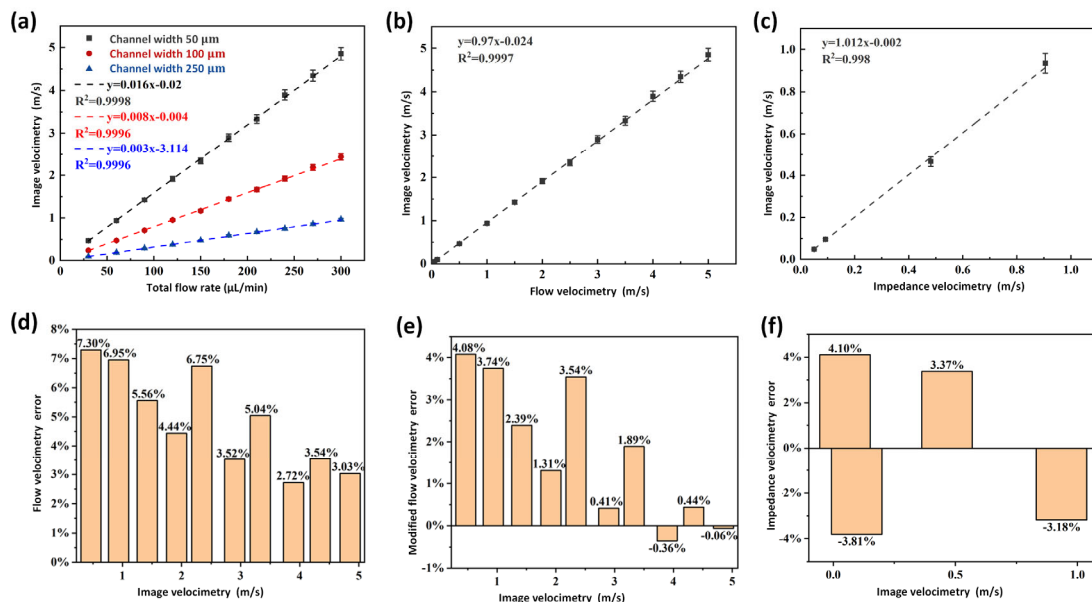

Fig. S10 Comparison of different velocimetry methods. (a) Relationship between image velocimetry and total flow rate in microchannels of different widths. (b) Fitted curves of image velocimetry and flow velocimetry in the 50 μm width microchannel. (c) Fitted curves of image velocimetry and impedance velocimetry. (d) Flow velocimetry error based on image velocimetry. (e) Flow velocimetry error corrected by a factor of 0.97. (f) Impedance velocimetry error based on image velocimetry.

Assuming that the image velocimetry is the real flow velocity, the image velocimetry (v_{image}) can be obtained according to the following formula:

$$v_{image} = \frac{D_{image}}{T_{image}} \tag{S23}$$

Where D_{image} is the distance that the sample moves between the images of two adjacent frames. T_{image} is the time difference between two adjacent frames. The image velocimetry is proportional to the total flow rate, as shown in Fig. S10a. The flow velocity calculated based on the total flow rate is basically consistent with the image velocimetry, and the fitting coefficient (R^2) is close to 1, as shown in Fig. S10b. Generally, the velocity of particles in a fluid is lower than the fluid's velocity due to the drag force exerted by the fluid. The particle velocity is primarily determined by the fluid velocity. For small and dense particles, their velocity tends to approach the fluid velocity, a concept explained by the Stokes number. The flow velocimetry (v_{flow}) can be obtained according to the following formula:

$$v_{flow} = \frac{Q_{total}}{WH} \tag{S24}$$

Where Q_{total} is the total flow rate of syringe pump, which is equal to the sum of the flow rates of sample flow and sheath flow. W and H are the width and height of microchannel in the detection area, respectively. Assuming a microchannel width of 50 µm, W and H are 50 µm and 20 µm, respectively. Due to the excessively high flow velocimetry, a correction coefficient of 0.97 must be applied to the flow velocimetry. With this correction, the flow velocimetry error is reduced to less than 5%, as shown in Fig. S10d & S10e. The flow velocimetry error (δv_{flow}) can be calculated using the following formula:

$$\delta v_{flow} = \frac{v_{flow} - v_{image}}{v_{image}} \times 100\% \tag{S25}$$

Where v_{flow} and v_{image} are flow velocimetry and image velocimetry, respectively. In addition, impedance velocimetry can also be performed through differential three-electrode. The accuracy of impedance velocimetry depends on the electrode preparation process and the sampling rate of impedance detection, which is limited by the USB data transfer rate. Therefore, impedance velocimetry is detected up to a maximum of 1 m/s. Moreover, due to the single syringe pump's minimum flow rate of 0.8 µL/min, impedance velocimetry is detected down to a minimum of 0.05 m/s. The impedance velocimetry is basically consistent with image velocimetry, as shown in Fig. S10c. The impedance velocimetry (v_{imp}) can be calculated by the following formula:

$$v_{imp} = \frac{D_{ele\_gap}}{T_{peak\_trough}} \tag{S26}$$

Where D_{ele_gap} is the gap distance of the differential three electrodes. Here, D_{ele_gap} is 50 µm. T_{peak_valley} is the time difference between the peak and valley of impedance signal. The impedance velocimetry error (δv_{imp}) can be calculated using the following formula:

$$\delta v_{imp} = \frac{v_{imp} - v_{image}}{v_{image}} \times 100\% \tag{S27}$$

Where v_{imp} and v_{image} are impedance velocimetry and image velocimetry, respectively. Both impedance velocimetry and corrected flow velocimetry errors are within ±5%, as shown in Fig. S10e & S10f, indicating the informative nature of both methods.

According to the above flow velocity prediction method, the impedance detection related parameters can be summarized, as shown in Table S2.

Table S2 Impedance detection related parameters

Flow velocity (m/s)	Total flow rate (µL/min)	f_{Sa} (kSa/s)	TC (µs)	R1=R2 (kV/A)	G1=G2
1	60	200	3	10	1
5	300	1,000	0.7832	100	1

In Table S2, f_{Sa} and TC are sampling rate and time constant of the lock-in amplifier. R and G are transimpedance gain and voltage gain of transimpedance amplifier. The total flow rate is equal to the sum of the flow rates of sample flow and sheath flow, and the flow rate ratio of sample flow to sheath flow is 2: 1. According to the formula (S14), the flow velocity of the sample can be predicted based on the total flow rate, as shown in Fig. S8.

The default flow velocity of particles or cells during impedance detection is 1 m/s, and the relevant parameters are set as follows: R1=R2=10 kV/A and G1=G2=1 for transimpedance amplifier, dual-frequency detection sampling rate of 230 kSa/s for lock-in amplifier, time constant of 3 µs for 8th-order low-pass filter, and adjustment of syringe pump flow rate so that the flow rates of sheath and sample streams are 40 µL/min and 20 µL/min, respectively. When the microchannel width in the detection area was 50 µm, the flow velocity in the detection area was about 1 m/s.

Due to the performance of the lock-in amplifier and sampling accuracy, the maximum flow velocity is 5 m/s. At this time, the setup utilized a transimpedance amplifier with R1=R2=100 kV/A and G1=G2=1, a lock-in amplifier dual-frequency detection sampling rate of 1 MSa/s, and an 8th-order low-pass filter time constant of 0.7832 µs. Adjusting the sheath flow and sample flow rates to 200 µL/min and 100 µL/min, respectively, with a microchannel width of 50 µm resulted in a flow velocity of approximately 5 m/s.

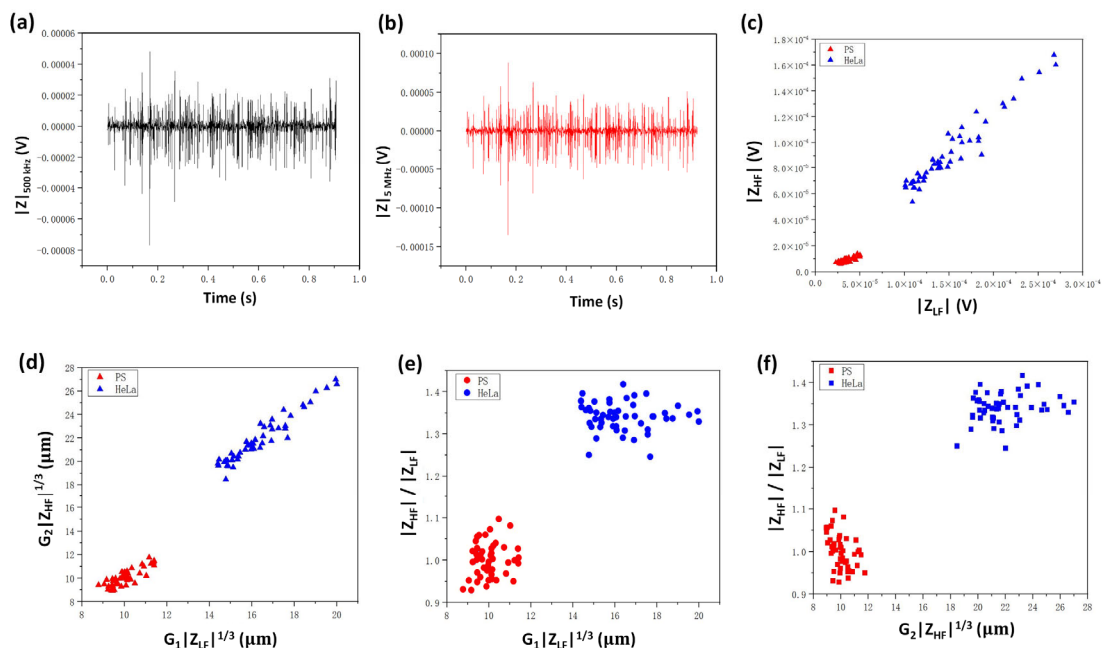## Section 7 Normalized characteristics of cells

Fig. S11 Normalized characteristics of cells. (a) and (b) are low-frequency amplitude and high-frequency amplitude of Hela cells after baseline cancellation, respectively. (c) Scatter plot of high-frequency amplitude versus low-frequency amplitude of Hela cells and 10 µm PS beads. (d) Normalized Hela cells using 10 µm PS beads. (e) Scatter plot of opacity versus low-frequency normalized electrical size. (f) Scatter plot of opacity versus high-frequency normalized electrical size.

In Fig. S11a & S11b, dual-frequency impedance detection was performed. In Fig. S11c & S11d, the electrical diameter of the cells was normalized from the impedance signal of the PS beads. The amplitude of the PS beads is first rooted three times ($|Z|1/3$) and multiplied by a factor ($G|Z|1/3$) so that the average of the samples is the diameter of the PS beads. This coefficient is then carried over to the amplitude of the cell after opening the root sign three times to obtain the normalized cell diameter.

In Fig. S11e, the average value of the low-frequency normalized cell diameter is approximately 16 µm, which aligns well with reality. However, in Fig. S11f, the average value of the high-frequency normalized cell diameter is about 22 µm, which deviates from reality. This suggests that normalized low-frequency impedance signals reflect cell size, while normalized high-frequency impedance signals are more sensitive to electrochemical properties such as cell membrane capacitance and cytoplasmic resistance.

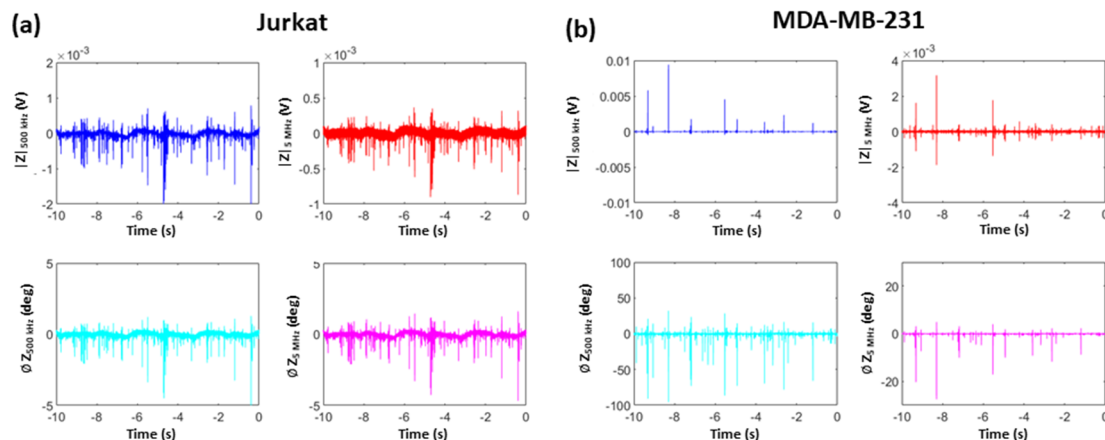## Section 8 Classification of Jurkat and MDA-MB-231 cells

Fig. S12 Impedance signals of Jurkat and MDA-MB-231 cells after de-baselining. (a) Amplitude and phase of Jurkat cells at 500 kHz and 5 MHz excitation signals. (b) Amplitude and phase of MDA-MB-231 cells at 500 kHz and 5 MHz excitation signals. Generally, dual-frequency impedance detection is used to study the classification basis, and finally the sorting is carried out based on the best classification basis. The impedance signals of the Jurkat and the MDA-MB-231 cells were subjected to a baseline elimination operation in order to facilitate comparison with each other. It can be observed that it is more obvious to distinguish Jurkat and MDA-MB-231 cells by phase than by amplitude.

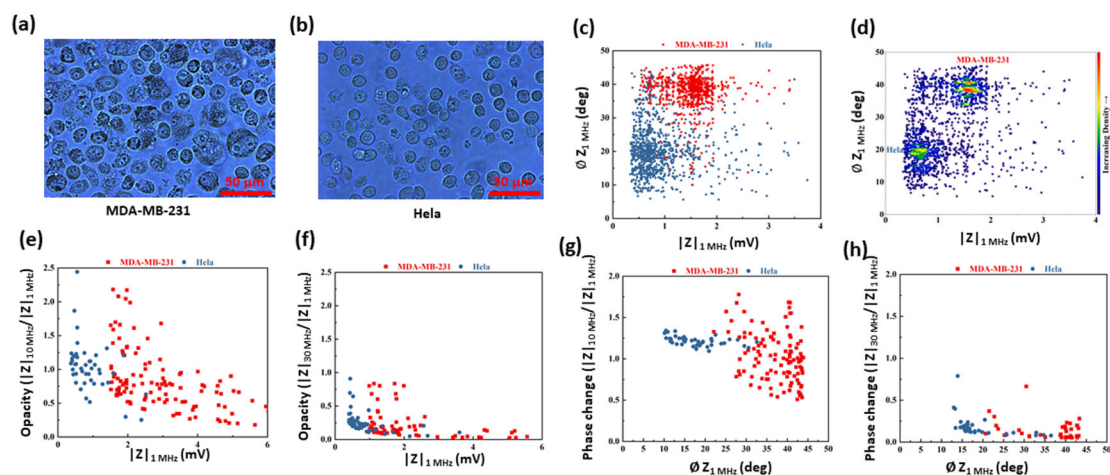## Section 9 Classification of Hela and MDA-MB-231 cells

Fig. S13 Classification of Hela and MDA-MB-231 cells. (a) Microimaging of MDA-MB-231 cells. (b) Microimaging of Hela cells. (c) Scatterplot. (d) Point density plot with dashed lines representing classification thresholds. 1,000 samples were counted for each. (e) and (f) are scatter plots of opacity ($|Z|_{10MHz}/|Z|_{1MHz}$), ($|Z|_{30MHz}/|Z|_{1MHz}$) versus $|Z|_{1MHz}$ amplitude, respectively. (g) and (h) are scatter plots of phase change ($|Z|_{10MHz}/|Z|_{1MHz}$), ($|Z|_{30MHz}/|Z|_{1MHz}$) versus $|Z|_{1MHz}$ phase, respectively.

In Fig. S13a & S13b, it can be observed that the morphology and distribution of intracellular components of MDA-MB-231 cells and Hela cells are similar, and some MDA-MB-231 cells have larger sizes. In Fig. S13c & S13d, the classification accuracy based on either amplitude or phase is approximately 80% due to the small size difference between MDA-MB-231 cells and HeLa cells. Therefore, further studies are needed to investigate whether impedance signals at different frequencies can effectively distinguish between MDA-MB-231 cells and HeLa cells.

In Fig. S13e-h, two representative results are illustrated here from the impedance detection results from 0.5 MHz to 50 MHz for opacity and phase changes of $|Z|_{10\,MHz}/|Z|_{1\,MHz}$ and $|Z|_{30\,MHz}/|Z|_{1\,MHz}$, respectively. The classification

of opacity and phase change is not significantly optimized compared to the classification of magnitude and phase. This suggests that MDA-MB-231 cells and HeLa cells have similar electrochemical characteristics and similar intracellular components, which can provide an effective basis for classification using deep learning methods such as support vector machines (SVMs) or long short-term memory networks (LSTMs).
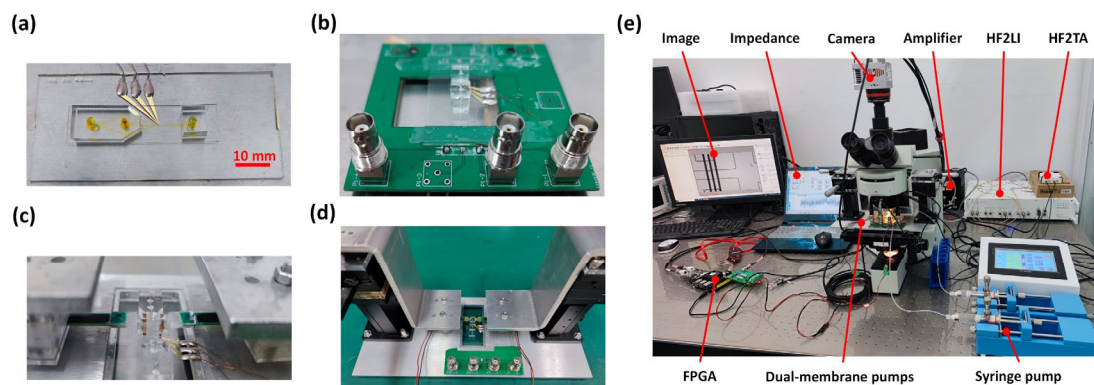
Section 10 Experimental platforms

Fig. S14 Experimental platforms. (a) Physical drawing of the impedance detection chip. (b) PCB device for impedance detection. (c) Enlarged view of the dual membrane pumps. (d) impedance-activated cell sorting device. (e) Physical drawing of the impedance-activated cell sorting system.

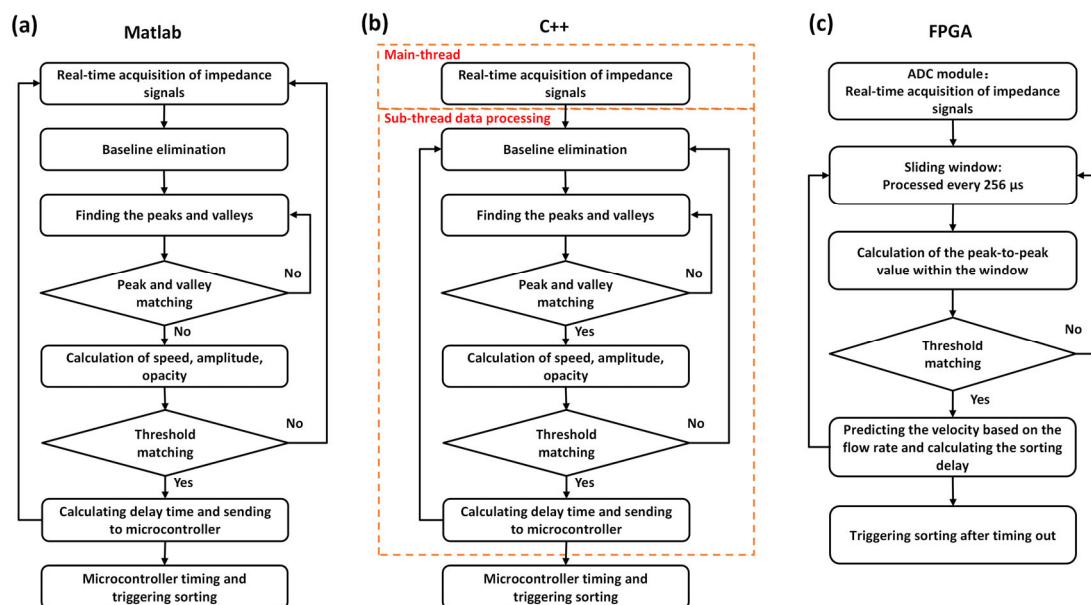## Section 11 Comparison of different data processing methods

Fig. S15 Flowcharts of different data processing methods. (a) Matlab single-thread data processing. (b) C++ dual-thread data processing. (c) FPGA parallel computing data processing.

Matlab, C++, and FPGA are utilized for data acquisition and processing to enhance throughput and reduce latency in data transmission. Matlab single-thread processing of 200 samples takes about 20 ms, while C++ dual-thread processing of 6,000 samples takes about 3 ms. FPGA parallel computing processing of 30,000 samples takes about 1 ms. The sorting scheme based on FPGA parallel computing can perform data acquisition and processing simultaneously, with faster data processing speed and low latency. Therefore, the FPGA-based sorting scheme is employed in this system.

Section 12 FPGA source code for peak finding

```verilog
reg [DW-1:0] max_0;
reg [DW-1:0] min_0;
reg [AW-1:0] max_0_addr;
reg [AW-1:0] min_0_addr;
always @(posedge fpga_clk) begin
    if (flag_cnt_0 == 1 && cnt_0 == 0) begin
        max_0 <= rd_data_0;         // Initialize max value with the current data
        min_0 <= rd_data_0;         // Initialize min value with the current data
        max_0_addr <= cnt_0;        // Initialize max value position
        min_0_addr <= cnt_0;        // Initialize min value position
    end
    else if (flag_cnt_0 == 1 && cnt_0 > 0) begin
        if (rd_data_0 > max_0) begin
            max_0 <= rd_data_0;     // Update max value
            max_0_addr <= cnt_0;    // Update max value position
        end
        else if (rd_data_0 < min_0) begin
            min_0 <= rd_data_0;     // Update min value
            min_0_addr <= cnt_0;    // Update min value position
        end
    end
end
reg [DW-1:0] max_1;
reg [DW-1:0] min_1;
reg [AW-1:0] max_1_addr;
reg [AW-1:0] min_1_addr;
always @(posedge fpga_clk) begin
    if (flag_cnt_1 == 1 && cnt_1 == 0) begin
        max_1 <= rd_data_0;         // Initialize max value with the current data
        min_1 <= rd_data_0;         // Initialize min value with the current data
        max_1_addr <= cnt_1;        // Initialize max value position
        min_1_addr <= cnt_1;        // Initialize min value position
    end
    else if (flag_cnt_1 == 1 && cnt_1 > 0) begin
        if (rd_data_0 > max_1) begin
            max_1 <= rd_data_0;     // Update max value
            max_1_addr <= cnt_1;    // Update max value position
        end
        else if (rd_data_0 < min_1) begin
            min_1 <= rd_data_0;     // Update min value
            min_1_addr <= cnt_1;    // Update min value position
        end
```

```
        end
end
parameter THRESHOLD = 125;                // Vpp peak-to-peak value > threshold. 256 corresponds to 10V. When
the gain is 10k, the threshold 1 corresponds to 39mV. Threshold 10 corresponds to 39uV.
reg [DW-1:0] Vpp;
reg [AW-1:0] App;                         // Position of the peak-to-peak value
always @(posedge fpga_clk) begin          // if must have else, otherwise latch may be generated, affecting circuit
stability.
    if (rd_en_0 == 1 && cnt_0 == DATA_DEPTH - 1) begin
        Vpp <= max_0 - min_0;
        App <= (max_0_addr > min_0_addr) ? (max_0_addr - min_0_addr) : (min_0_addr - max_0_addr);
    end
    else if (rd_en_0 == 1 && cnt_1 == DATA_DEPTH - 1) begin
        Vpp <= max_1 - min_1;
        App <= (max_1_addr > min_1_addr) ? (max_1_addr - min_1_addr) : (min_1_addr - max_1_addr);
    end
end
```
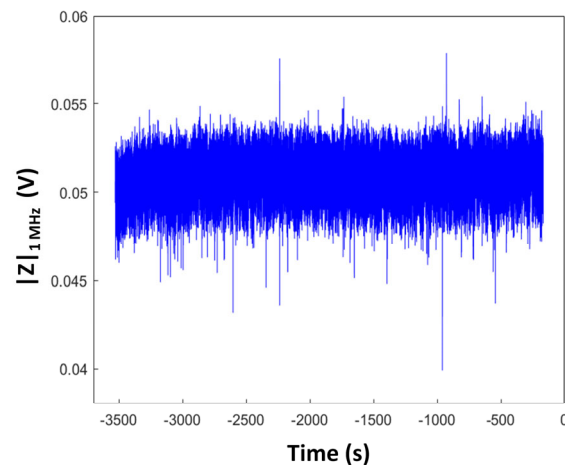
Section 13 Stability test

Fig. S16 Amplitude of PS beads under 1 MHz excitation signal at about 1 m/s for 1 hour.

By introducing PEG6000 into both the sheath and sample, the settling rate of particles can be reduced. This addition increases the viscosity of the non-conducting sheath and sample, consequently enhancing the signal-to-noise ratio and signal stability[3]. These improvements contribute to the overall stability of impedance detection and reduce baseline drift. As illustrated in Fig. S16, this system demonstrates the ability to conduct high-throughput detection and sorting reliably for extended durations, up to several hours.

Supplementary movies

Movie S1. Sorting of 15 μm PS beads from a mixed sample to the collection port based on amplitude with high-throughput and high-accuracy.

Movie S2. Sorting of 7 μm PS beads into the collection port based on phase with high-throughput and high-accuracy.

Notes and references

1. A. Gross, J. Schondube, S. Niekrawitz, W. Streule, L. Riegger, R. Zengerle and P. Koltay, J Lab Autom, 2013, 18, 504-518.
2. Y. Xu, X. Xie, Y. Duan, L. Wang, Z. Cheng and J. Cheng, Biosens Bioelectron, 2016, 77, 824-836.
3. J. Zhu, Y. Feng, H. Chai, F. Liang, Z. Cheng and W. Wang, Lab Chip, 2023, 23, 2531-2539.